Journal of
Mechanics of
Materials and Structures

A NONLINEAR MICROMECHANICAL MODEL FOR PROGRESSIVE DAMAGE OF VERTEBRAL TRABECULAR BONES

Eyass Massarwa, Jacob Aboudi, Fabio Galbusera, Hans-Joachim Wilke and Rami Haj-Ali

msp

∎
∎msp

A NONLINEAR MICROMECHANICAL MODEL FOR PROGRESSIVE DAMAGE OF VERTEBRAL TRABECULAR BONES

EYASS MASSARWA, JACOB ABOUDI, FABIO GALBUSERA,
HANS-JOACHIM WILKE AND RAMI HAJ-ALI

A new three-dimensional (3D) nonlinear micromechanical analysis is proposed to predict the overall mechanical response to damage evolution of the vertebral trabecular bone (VTB) highly porous microstructure. Towards that goal, a nonlinear micromechanical model, based on the 3D parametric high fidelity generalized method of cells (HFGMC) micromechanics, is extended to include progressive damage. The damage is initiated at the local subcell and its evolution is carried out using a strain-softening method. The nonlinear HFGMC behavior including damage evolution is first verified by examining its ability to predict the experimental nonlinear compression stress-strain response of printed polymeric VTB highly porous microstructure. Next, predicted HFGMC pre- and postultimate failure for native VTB representative unit cells (RUCs) harvested from different vertebrae of human cadavers (n = 10) are carried out. Some of the latter predictions were compared to reported values found in the literature. The proposed nonlinear HFGMC micromechanical model with evolving damage can predict the overall nonlinear behavior, including postultimate range.

1. Introduction

Osteoporosis is a bone disease state characterized by low bone strength and an increased fracture risk of the bone walls. Although osteoporosis affects the entire skeleton, osteoporotic fractures commonly occur in the spine vertebrae [Nevitt et al. 1999]. The vertebral bodies, primary structures located in the spine, bear the compressive loads. Vertebrae are composed of an internal highly porous trabecular bone core surrounded by a thin shell of dense material called cortical bone [Cowin 2001]. Studies have shown that the trabecular bone carries a substantial proportion of the compressive loads applied to the vertebral body [Rockoff et al. 1969]. The loss of trabecular bone density and strength throughout the osteoporotic process leads to failure of the entire vertebra. Maquer et al. [2015] showed that osteoporotic vertebral compression fractures strongly depend on bone volume fraction and trabecular bone microarchitecture.

Experimental studies with irreversible loading (overloading and damage) of the trabecular bone have been conducted. A reduction of the elastic moduli, strength and accumulation of residual deformations in the trabecular bone were the main consequences [Keaveny et al. 1994; 1999; Zysset 1994]. Another extensive experimental outcome demonstrated that for postyield behavior, the yield strains over a limited range of densities for human vertebral trabecular bones (VTBs) are independent of the apparent density and have reasonably constant values [Kopperdahl and Keaveny 1998]. Another important study by Fyhrie et al. [1994] microscopically examined the mechanisms of failure in human VTBs compressed by a large

deformation. Microscopic cracking as the result of shear stresses in the trabeculae, complete fractures of trabeculae occurring in those oriented transversely to the loading direction and residual compressive strain formation were the main observations of this study. Based on other experimental studies [Fyhrie and Schaffler 1994; Gibson and Ashby 1999; Hayes and Carter 1976], the load-displacement curves for VTB specimens can include a sequence of several responses:

(1) an initial linear undamaged region;

(2) a material nonlinear response including strain-softening caused by damage accumulation;

(3) ultimate load peak region;

(4) postpeak unloading with increased strain and displacement; and

(5) a region where with increased displacements, the load is increased with very small values.

Finite element models have been extensively used to study trabecular bone mechanical behavior due to the anatomical complexity of the trabecular bone and limited availability of cadaveric specimens. A previous study [Niebur et al. 2000] presented a nonlinear high-resolution finite element analysis framework to calibrate the effective elastic moduli, as well as tensile and compressive yield strains of the bovine tibia trabecular bone. In another study, based on a voxel-based finite element analysis combined with physical measurements of volume fraction, μCT reconstructions, uniaxial mechanical and nanoindentation tests of trabecular bone extracted from cadaveric proximal femurs was demonstrated [Chevalier et al. 2007]. More recently, Hamed and Jasiuk [2013] introduced a multiscale computational finite element model with dominant damage mechanisms to predict stiffness and bone strength at different structural scales by using cohesive interface elements. Harrison et al. [2013] also developed a 3D high-resolution model with fracture criteria and a large-deformation computational model predicting the full range of response including the pre- and postultimate stress state, referred to as "ultimate strength" by the authors. The damage and fracture processes were simulated at the local element by reducing the elastic modulus and removing the element, respectively. This analysis model has successfully predicted ultimate strength following the softening of the trabecular bone. In order to analyze human trabecular bone samples under compressive loading, an isotropic μCT finite element model coupled to a damage law was developed [Hambli 2013]. The element deletion technique was also adapted.

Goda et al. [2012] presented a micromechanical method to investigate the microstructural effects of the macroscopic mechanical properties of trabecular bones. A Cosserat anisotropic continuum model was modeled from the discrete homogenization of a quasiperiodical lattice model for the microstructural trabecular bone where the effective mechanical properties of the trabecular bone were directly related to the lattice microstructure and its elastic properties. In addition, the bone walls of the lattice were modeled as linear elastic Timoshenko thick beams. Recently, Goda and Ganghoffer [2015] introduced a three-dimensional model studying the multiaxial yield and failure response of trabecular bones and established criteria for brittle and ductile collapse based on micromechanical methods. In this study, the homogenization technique was used to create the plastic yield surfaces of two and three-dimensional bending-dominated periodic lattices which demonstrate the topology of trabecular bones. More recently, Goda et al. [2016] developed a numerical model to predict the effective properties of porous polymeric biomaterials. Finite element models based on an accurate three-dimensional solid model from μCT data were generated to quantify the effects of the porosity. In this study, the second gradient of deformation,

which is expressed as in couples stress continuum theories, was used to address the size dependency in porous structures.

The high fidelity generalized method of cells (HFGMC) is a micromechanical method used to analyze 2 and 3D multiphase composites. Global and local quadratic displacement fields (microvariables) within a discretized representative volume element (RVE) divided into subcells are applied. The mechanical formulation of the HFGMC is performed using traction and displacement continuity equations between the interfaces of the subcells as well as the average volume equilibrium applied in the subcells [Haj-Ali and Aboudi 2013, 2016]. The HFGMC method has been widely used for both linear and nonlinear applications in order to analyze the behavior of multiphase composites such as viscoelastic, viscoplastic, bond damage of fiber, smart composite materials and piezoresistive fiber-reinforced composites [Aboudi et al. 2013; Haj-Ali et al. 2014]. The HFGMC method with damage evolution effects has also been proposed [Haj-Ali and Aboudi 2009] using cohesive traction-separation between the subcells and cell extinction damage (CED) approaches.

In the present study, to predict the overall nonlinear mechanical response with evolving damage of VTB highly porous microstructures, a proposed nonlinear 3D parametric HFGMC with progressive damage is presented. Verification of the model is performed by comparing the nonlinear stress-strain predicted curve to one obtained from our own compression tests performed on a printed polymeric VTB-RUC microstructure as well as curves reported in the literature for native VTBs.

2. Methods

A nonlinear micromodeling framework based on the 3D parametric HFGMC micromechanical method was formulated to predict the nonlinear response including damage evolution of a VTB highly porous microstructure deformed under a uniaxial compression stress state [Haj-Ali and Aboudi 2013, 2016]. A nonlinear elastic power-law model and postfailure approach were used. Three-dimensional μCT HFGMC models were geometrically generated from scanned specimens. In addition, compression tests
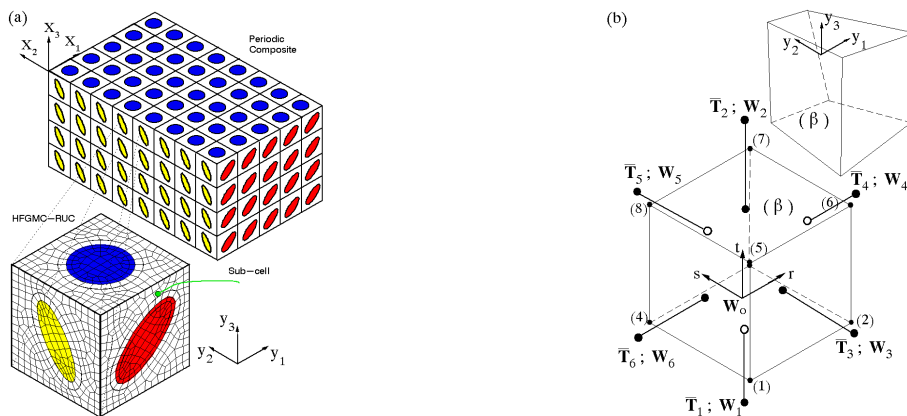
Figure 1. Schematic illustration of a triply periodic multiphase composite material in the global coordinate system with its HFGMC representative unit cell (RUC) comprising general hexahedral subcells defined with respect to its local coordinate system, (a). A general hexahedral subcell in its physical and parent coordinate systems, (b).

on 3D printed polymeric VTB-RUC microstructures were conducted to generate its stress-strain response and verify the ability of the nonlinear HFGMC model to predict nonlinear VTB behavior.

2.1. *Nonlinear HFGMC model.* We present herein the mechanical formulation of the nonlinear parametric HFGMC based on Haj-Ali and Aboudi's studies [2013; 2016]. The parametric HFGMC micromechanical method is based on the homogenization technique, in which a representative unit cell (RUC) of a triply periodic multiphase composite can be identified. A multiphase composite of a triply periodic microstructure defined with respect to the global coordinate system (X_1, X_2, X_3) is schematically described together with its parallelepiped RUC and defined with respect to the local material coordinate system (y_1, y_2, y_3) (Figure 1a). The RUC domain is discretized into a general assembly of hexahedral subcells representing different phase geometries. A general hexahedral subcell is mapped to a uniform parametric coordinate system (r, s, t) using a classical linear transformation (Figure 1b). The compact quadratic form of the increment of the displacement vector Δu in each subcell is defined by

$$
\begin{aligned}
\Delta u = \Delta u^0 + \Delta W_0 &+ \tfrac{1}{2}(\Delta W_4 - \Delta W_6)r + \tfrac{1}{2}(\Delta W_5 - \Delta W_3)s + \tfrac{1}{2}(\Delta W_2 - \Delta W_1)t \\
&+ \tfrac{1}{4}(\Delta W_4 + \Delta W_6 - 2 \cdot \Delta W_0)(3r^2 + rs + rt - 1) \\
&+ \tfrac{1}{4}(\Delta W_3 + \Delta W_5 - 2 \cdot \Delta W_0)(3s^2 + rs + st - 1) \\
&+ \tfrac{1}{4}(\Delta W_1 + \Delta W_2 - 2 \cdot \Delta W_0)(3t^2 + rt + st - 1),
\end{aligned}
\tag{1}
$$

where the applied remote global increment of the displacement field is $\Delta u^0 \equiv \Delta \varepsilon^0 \cdot X$. Here, ε^0 is the applied remote second order strain tensor.

The components of vectors ΔW_k, $k = 1 \ldots 6$ and one additional internal displacement variable ΔW_0 are the increments of the fluctuating displacement microvariables. The strain vector

$$
\varepsilon^T \equiv \{\varepsilon_{11}, \varepsilon_{22}, \varepsilon_{33}, 2\varepsilon_{23}, 2\varepsilon_{13}, 2\varepsilon_{12}\}
$$

in a given subcell (β) is defined in an incremental form by

$$
\Delta \varepsilon_{ij}^{(\beta)}(y(r, s)) = \Delta \varepsilon_{ij}^0 + \frac{1}{2}\left(\frac{\partial(\Delta u_i)}{\partial y_j} + \frac{\partial(\Delta u_j)}{\partial y_i}\right),
\tag{2}
$$

$$
\Delta \varepsilon^{(\beta)} = \Delta \varepsilon^0 + A^{(\beta)} \Delta W^{(\beta)},
\tag{3}
$$

where $A^{(\beta)}$ is the matrix relating to the incremental strain displacement microvariables. The nonzero components of this matrix are found in Haj-Ali and Aboudi's studies [2013; 2016]. The increment of the displacement microvariables vector $\Delta W^{(\beta)}$ of the subcell (β) includes 21 components.

For a general nonlinear material filling a subcell (β), the incremental form of its constitutive relationship is given by

$$
\Delta \sigma^{(\beta)} = C^{t,(\beta)} : \Delta \varepsilon^{(\beta)},
\tag{4}
$$

where $C^{t,(\beta)}$ is the proper instantaneous fourth-order tangential stiffness tensor that is computed based on the considered nonlinear material response within the subcell. The incremental stress and strain vectors of a subcell (β) are $\Delta \sigma^{(\beta)}$ and $\Delta \varepsilon^{(\beta)}$, respectively.

The incremental surface-average traction vector on face number k of the hexahedral subcell (β) is then obtained by the following equation:

$$\Delta \bar{T}^{(\beta_k)} = \tfrac{1}{4} N^{(\beta_k)} \Delta C^{t,(\beta)} [\Delta \varepsilon^0 + \bar{A}^{(\beta_k)} \Delta W^{(\beta)}], \tag{5}$$

where the $N^{(\beta_k)}$ matrix is defined by

$$N^{(\beta_k)} = \begin{bmatrix} n_1 & 0 & 0 & 0 & n_3 & n_2 \\ 0 & n_2 & 0 & n_3 & 0 & n_1 \\ 0 & 0 & n_3 & n_2 & n_1 & 0 \end{bmatrix}^{(\beta_k)}. \tag{6}$$

The (n_1, n_2, n_3) are the components of the normal vector to the k-th face of subcell (β). Matrix $\bar{A}^{(\beta_k)}$ is computed as

$$\bar{A}^{(\beta_k)} = \int_{-1}^{1} \int_{-1}^{1} A^{(\beta)} \, dr \, ds. \tag{7}$$

Next, we impose traction and displacement interfacial continuity conditions within the inner subcells:

$$\begin{aligned} \Delta \bar{T}^{(\beta_k)} &= \Delta \bar{T}^{(\gamma_m)}, \\ \Delta W_k^{(\beta)} &= \Delta W_m^{(\gamma)}. \end{aligned} \tag{8}$$

This is done using the incremental surface-average microvariables. In addition, equilibrium equations of each subcell are applied in an incremental volumetric average form:

$$\int_V \nabla \cdot (\Delta \sigma) \, dV = \sum_{k=1}^{6} A_k \Delta \bar{T}^{(\beta_k)} = 0. \tag{9}$$

Here, (β_k) denotes the k-th face of subcell (β), (γ_m) is the neighboring m-th face of subcell (γ), v_β is the volume of subcell (β) and A_k is the area of the k-th face.

The total number of unknown incremental displacement microvariables in the RUC is $21 \times N_c$, where N_c is the total number of subcells (each one having 21 displacement microvariables). The number of continuity equations for incremental displacements is $3 \times 3N_c$ (for each subcell there are only three independent interfaces). The number of incremental traction continuity equations is also $3 \times 3N_c$. The incremental volume average equilibrium equations in (9) present an additional $3N_c$ equations.

The assembly of the derived $21N_c$ HFGMC governing equations of the RUC can be symbolically expressed by

$$[\Delta R] \equiv \begin{bmatrix} \Delta T^{(+)} - \Delta T^{(-)} \\ \Delta W^{(+)} - \Delta W^{(-)} \\ \int_V \nabla \cdot (\Delta \sigma) \, dV \end{bmatrix} = 0, \quad \{D\} \equiv \begin{Bmatrix} D_T \\ 0 \\ 0 \end{Bmatrix}, \tag{10}$$

where $[\Delta R]$ is the incremental residual matrix expressing the incremental form of the displacement continuity, traction continuity and subcells' equilibrium, respectively.

The 21 unknown incremental displacement microvariables for each subcell (β) are obtained by solving the system of linear equation resulting from the linearized incremental form of (10). In general, the

governing incremental equations can symbolically be written as

$$\{\Delta W\} = -[\partial(\Delta R)/\partial(\Delta W)]^{-1} \cdot \{D\} \cdot \{\Delta \bar{\varepsilon}^0\}. \tag{11}$$

Then, the above system is solved for a given incremental remote applied strain vector $\Delta \bar{\varepsilon}^0$ in order to obtain the incremental displacement microvariables of the subcells. Moreover, the incremental local strain vectors can be readily obtained using (3), leading in turn to the spatial distribution of the incremental stresses in the RUC. Further discussion of the solution approach for the above equation system and how to obtain the overall tangential stiffness matrix of a multiphase composite can be found in Haj-Ali and Aboudi's research [2013; 2016].

2.2. Material nonlinearity. A nonlinear elastic power-law model of the Ramberg–Osgood (R-O) strain-stress relationship is used to reflect the softening of the bone wall tissue material [Hambli 2013; Keaveny et al. 2003]. To this end, a nonlinear response of an isotropic and reversible material is modeled [Haj-Ali and Aboudi 2009; Haj-Ali and Kilic 2003; Khan and Huang 1995] using the general multiaxial form of the R-O representation as follows:

$$\varepsilon_{ij} = \varepsilon_{ij}^e + \varepsilon_{ij}^p = \left(\frac{1+v}{E} + \frac{3\alpha}{2E}\left(\frac{\sigma_e}{\sigma_0}\right)^{n-1}\right) \cdot s_{ij} + \frac{\sigma_{kk}}{9K}\delta_{ij}, \tag{12}$$

where the Young's modulus is E, Poisson's ratio is v, $K = E/[3(1-2v)]$ and α, σ_0, n are the material constants and ε_{ij} is the total strain tensor, ε_{ij}^e is the elastic strain components, ε_{ij}^p is the plastic strain components and σ_{ij}, s_{ij} are the stress and stress deviatoric tensors, respectively. Kronecker's delta tensor is δ_{ij} and σ_e is the equivalent stress as follows:

$$\sigma_e = \sqrt{\tfrac{3}{2} \cdot s_{ij} \cdot s_{ij}}. \tag{13}$$

To this end, the incremental strain-stress relationship in vector notation is

$$\Delta \varepsilon = (S^e + \phi \cdot P + \alpha_t \cdot \phi \cdot \hat{s} \cdot \hat{s}^T)\Delta \sigma = S_t \Delta \sigma, \tag{14}$$

where the linear elastic compliance matrix for an isotropic material is $S^e (6 \times 6)$, $\hat{s}(6 \times 1)$ is the stress deviatoric vector and $S_t(6 \times 6)$ is the tangent compliance matrix. We also have:

$$\phi = \frac{3\alpha}{2E}\left(\frac{\sigma_e}{\sigma_0}\right)^{n-1},$$

$$\alpha_t = \tfrac{3}{2}(n-1) \cdot \frac{1}{\sigma_e^2},$$

$$P = \frac{1}{3}\begin{bmatrix} 2 & & & & & \\ -1 & 2 & & & \text{Symm.} & \\ -1 & -1 & 2 & & & \\ 0 & 0 & 0 & 6 & & \\ 0 & 0 & 0 & 0 & 6 & \\ 0 & 0 & 0 & 0 & 0 & 6 \end{bmatrix}. \tag{15}$$

To this end, the tangent stiffness matrix is derived by inverting the tangent compliance matrix. Once the stress vector is given, the corresponding stain vector and the tangent stiffness matrix can be computed

using (12). But when the strain vector is provided, it should initially determine the equivalent stress (σ_e) by iteratively solving the following scalar nonlinear polynomial equation using the Newton–Raphson method to obtain the corresponding stress vector and tangent stiffness matrix:

$$\phi \cdot \sigma_e + \frac{1}{2G} \cdot \sigma_e - \varepsilon_e = 0. \tag{16}$$

The shear modulus $G = E/[2(1+v)]$, where ε_e is defined as the equivalent strain and is related to the deviatoric strain tensor (e_{ij}) as follows:

$$\varepsilon_e = \sqrt{\tfrac{3}{2} \cdot e_{ij} \cdot e_{ij}}. \tag{17}$$

2.3. *Damage response.* An isotropic damage model for postfailure stiffness degradation is used. When failure is detected, the relevant subcell is extinct. This progressive damage model is coupled with the HFGMC micromechanical model at the subcell level. To this end, the following isotropic damage model is adopted and imposed:

$$\boldsymbol{\sigma}^{(\beta)} = (1 - D^{(\beta)})\boldsymbol{C}^{t,(\beta)} : \boldsymbol{\varepsilon}^{(\beta)}, \tag{18}$$

where the current associated subcell damage variable is $0 \le D^{(\beta)} \le 1$ and $\boldsymbol{C}^{t,(\beta)}, \boldsymbol{\sigma}^{(\beta)}, \boldsymbol{\varepsilon}^{(\beta)}$ are the instantaneous tangent stiffness matrix, stress vector and strain vector of subcell (β), respectively. Damage variable in a subcell is governed by the equivalent strain ε_e; see (17). A linear relationship between the subcell damage variable $D^{(\beta)}$ and the equivalent strain $\varepsilon_e^{(\beta)}$ is assumed as follows:

$$\begin{cases} D^{(\beta)} = 0 & \text{if } 0 < \varepsilon_e^{(\beta)} < \varepsilon_e^{(\beta),\text{initial}}, \\ D^{(\beta)} = \dfrac{1}{1-\eta}\left(1 - \dfrac{\varepsilon_e^{(\beta)}}{\varepsilon_e^{(\beta),\text{initial}}}\right) & \text{if } \varepsilon_e^{(\beta)} > \varepsilon_e^{(\beta),\text{initial}}, \\ D^{(\beta)} = 1 & \text{if } \varepsilon_f = \eta\varepsilon_e^{(\beta),\text{initial}}, \end{cases} \tag{19}$$

where the parameter η is used to relate the equivalent strain damage $\varepsilon_e^{(\beta),\text{initial}}$ to the final strain ε_f when the subcell is extinct (removed, no stiffness). Its limit values ($\eta = 1, \infty$) correspond to highly brittle and highly ductile states, respectively. Once the damage variable is initiated, a strain softening scheme is imposed whereby the stiffness of the subcell is degraded. Herein, damage initiates at the subcell once the failure is detected according to

$$\sigma_e^{(\beta)} \ge X, \tag{20}$$

where $\sigma_e^{(\beta)}$ is the equivalent stress at subcell (β) and X is a calibrated value denoting the effective strength value of the bone wall constituent.

2.4. *Nonlinear implementation.* To this end, an incremental solution algorithm using the 3D nonlinear parametric HFGMC, a nonlinear material model and a damage approach is developed. The numerical algorithm proceeds incrementally for a given number of increments n_{inc} as shown on the next page. Once given the history of total stress and strain vectors in the subcells (Step 2.1), the prior local tangent stiffness matrices of the subcells $\overline{\boldsymbol{C}}_{i-1}^{t,(\beta)}$ (Step 2.2) and the overall prior tangential stiffness matrix $\overline{\boldsymbol{C}}_{i-1}^{t}$ (Step 2.3), can be computed. Next, the current remote incremental average strain vector $\{\Delta\bar{\boldsymbol{\varepsilon}}^0\}_i = \{\Delta\bar{\varepsilon}_a, \Delta\bar{\varepsilon}_b\}_i$

Incremental solution algorithm

1 Initialize parameters: n_{inc}, $\boldsymbol{\sigma}_0^{(\beta)} = \{0\}$, $\boldsymbol{\varepsilon}_0^{(\beta)} = \{0\}$, $\Delta\bar{\varepsilon}_a$, X

2 WHILE $i \leq n_{\text{inc}}$ DO

  2.1 Recall prior total local stress $\boldsymbol{\sigma}_{i-1}^{(\beta)}$, strain $\boldsymbol{\varepsilon}_{i-1}^{(\beta)}$, and damage variable $D_{i-1}^{(\beta)}$.

  2.2 Compute prior tangent stiffness matrices $\boldsymbol{C}_{i-1}^{t,(\beta)}$.

  2.3 Compute prior global tangent stiffness matrix $\bar{\boldsymbol{C}}_{i-1}^t$.

  2.4 Using (21), get applied remote incremental average strain vector: $\{\Delta\bar{\boldsymbol{\varepsilon}}^0\}_i$

  2.5 Solve Eq. (11), $\{\Delta\boldsymbol{W}\}_i = -[\partial(\Delta\boldsymbol{R})/\partial(\Delta\boldsymbol{W})]_i^{-1} \cdot \{\boldsymbol{D}\}_i \cdot \{\Delta\bar{\boldsymbol{\varepsilon}}^0\}_i$, for the current incremental displacement microvariables.

  2.6 FOR $\beta = 1, 2, 3, \ldots, N_c$ DO

    2.6.1 Get current total local strain vector $\{\boldsymbol{\varepsilon}\}_i^{(\beta)} = \{\bar{\boldsymbol{\varepsilon}}^0\}_i + A_i^{(\beta)}\{\Delta\boldsymbol{W}\}_i^{(\beta)} + \{\boldsymbol{\varepsilon}\}_{i-1}^{(\beta)}$.

    2.6.2 Compute current tangent stiffness matrix $\boldsymbol{C}_i^{t,(\beta)}$.

    2.6.3 Using (18), perform constitutive calculations for total local stress vector $\{\boldsymbol{\sigma}\}_i^{(\beta)}$:

      IF $D_{i-1}^{(\beta)} \leq 1$ THEN

        $\{\boldsymbol{\sigma}\}_i^{(\beta)} = (1 - D_{i-1}^{(\beta)})\boldsymbol{C}_i^{t,(\beta)} : \{\boldsymbol{\varepsilon}\}_i^{(\beta)}$

      ELSE

        $\{\boldsymbol{\sigma}_i^{(\beta)}\} = \{0\}$, $\boldsymbol{\varepsilon}_i^{(\beta)} = \{0\}$, subcell (β) extinct

    2.6.4 Using (13), compute current total equivalent stress $\sigma_e^{(\beta),i}$.

      IF $\sigma_e^{(\beta),i} \geq X$ and $D_{i-1}^{(\beta)} = 0$ THEN

        Using (17), compute total equivalent strain for damage initiation: $\varepsilon_e^{(\beta),\text{initial}}$

    2.6.5 Using (17), compute current total equivalent strain: $\varepsilon_e^{(\beta),i}$

    2.6.6 Using (19), update current damage variable: $D_i^{(\beta)}$

  2.7 Compute RUC current total stress and strain vectors:

$$\{\bar{\boldsymbol{\sigma}}\}_i = \frac{1}{V}\int_V \{\boldsymbol{\sigma}\}_i \, dV = \frac{1}{V}\sum_{\beta=1}^{N_c} v_\beta \{\boldsymbol{\sigma}\}_i^{(\beta)}, \quad \{\bar{\boldsymbol{\varepsilon}}\}_i = \frac{1}{V}\int_V \{\boldsymbol{\varepsilon}\}_i \, dV = \frac{1}{V}\sum_{\beta=1}^{N_c} v_\beta \{\boldsymbol{\varepsilon}\}_i^{(\beta)}.$$

Set $i = i + 1$.

---

for the RUC, deformed under a uniaxial stress state, is evaluated (Step 2.4) by solving the following linearized equation system:

$$\begin{Bmatrix} \dfrac{\Delta\bar{\sigma}_a}{0} \\ 0 \\ 0 \\ 0 \\ 0 \end{Bmatrix}_i = \begin{bmatrix} \bar{C}_{aa}^t & \{\bar{\boldsymbol{C}}_{ab}^t\}_{1\times 5} \\ \{\bar{\boldsymbol{C}}_{ba}^t\}_{5\times 1} & [\bar{\boldsymbol{C}}_{bb}^t]_{5\times 5} \end{bmatrix}_{i-1} \cdot \begin{Bmatrix} \dfrac{\Delta\bar{\varepsilon}_a}{\{\Delta\bar{\boldsymbol{\varepsilon}}_b\}_{5\times 1}} \end{Bmatrix}_i,$$

$$\{\Delta\bar{\boldsymbol{\varepsilon}}_b\}_i = -[\bar{\boldsymbol{C}}_{bb}^t]_{i-1}^{-1} \cdot \{\bar{\boldsymbol{C}}_{ba}^t\}_{i-1} \cdot \Delta\bar{\varepsilon}_a,$$

$$\{\Delta\bar{\boldsymbol{\varepsilon}}^0\}_i = \{\Delta\bar{\varepsilon}_a, \Delta\bar{\boldsymbol{\varepsilon}}_b\}_i,$$

(21)

where $\Delta\bar{\boldsymbol{\varepsilon}}_a$ is a given average strain increment in the axial direction (11) of the RUC. In Step 2.5, the equation system (10) is established and solved with the current incremental $\{\Delta\bar{\boldsymbol{\varepsilon}}^0\}_i$ evaluating the current incremental microvariables $\{\Delta\boldsymbol{W}\}_i$; see (11). Then, for all the subcells in the given RUC, the current total local strain vector (Step 2.6.1), tangent stiffness matrix (Step 2.6.2) and stress vector (Step 2.6.3) are evaluated. Subsequently in Step 2.6.4, the equivalent stress is computed and compared with the calibrated value denoting the effective strength value of the bone wall constituent. Once the equivalent stress is greater than the calibrated effective strength value, the initial equivalent strain is computed and fixed. Next, the current total equivalent strain is computed (Step 2.6.5) and in Step 2.6.6, the current damage variable is updated according to the computed current total equivalent strain (19). The global stress and strain vectors are obtained in Step 2.7 and the algorithm proceeds to the next increment. It should be noted that there is no need to apply periodic boundary conditions in order to simulate the current axial loading which is directly imposed on the RUC. This special case yields zero average traction on the edges of the RUC. To that end, the microvariables at the edges are set to zero.

2.5. *Microcomputed tomography imaging.* Selected CT bone scans shown in Table 1 were acquired from a larger database originally reported by Wolfram et al. [2011] which included 104 (50 males, 54 females) fresh frozen human vertebrae (T1–L3) obtained from 32 donors (21–94y, median = 65) and stored at $-20°$ after harvest. Surrounding soft tissue was removed from the vertebrae, and the posterior structures were partially removed. Endplates were removed with a band saw. Subsequently, 251 cylindrical specimens (8 mm in diameter and 18–25 mm in height) were cored from the remaining slices by a custom-made core drill. Marrow was removed from the top and bottom of the cylinders using a pulsed waterjet (Braun Oral-B Professional Care 6500). The cylinders were submerged in water containing 0.9% sodium chloride and scanned in a μCT (μCT 40, SCANCO Medical AG) at a resolution of $12\,\mu\text{m}^3$.

2.6. *Damage analysis of vertebral trabecular bones.* 3D RUCs demonstrating the VTB highly porous microstructure were studied for nonlinear with damage response. Figure 3a represents a human vertebral body macroscale from which high resolution images of sequential and cylindrical cross sections of μCT scans were generated. By stacking the cross-sectional images, the original VTB microstructure can then be rebuilt as a 3D solid model (Figure 3b). The VTB-RUC has been arbitrarily selected with an approximate length of $l = w = h = 8.1 \pm 0.3$ mm. Then, the 3D solid model representing the bone walls (Figure 3c) and the marrow (soft fatty substances in the cavities of bones) domain (Figure 3d)

vertebral level	gender	age	vertebral level	gender	age
T11	F	43	T11	M	37
T12	F	43	T12	M	44
T12	F	46	T12	M	56
T11	F	60	T11	M	84
T12	F	60	L2	M	84
L3	F	80			

Table 1. Vertebrae scanned samples analyzed in this study reported in [Wolfram et al. 2011].
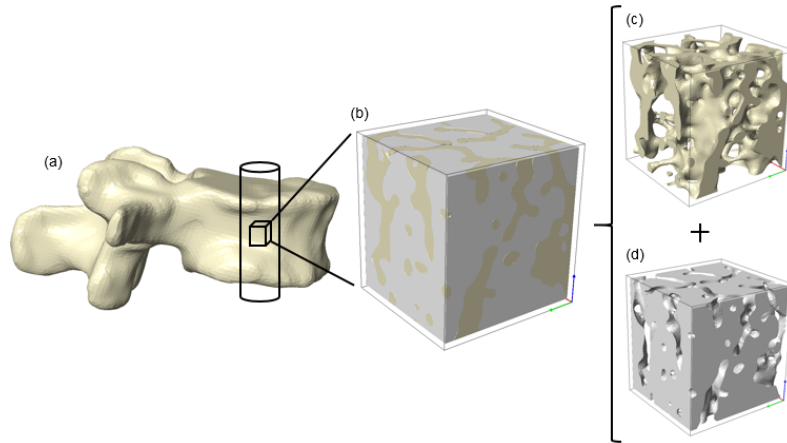
Figure 3. Human vertebral body (macroscale), (a); a VTB-RUC microstructure, (b); bone walls, (c), and marrow domain, (d).
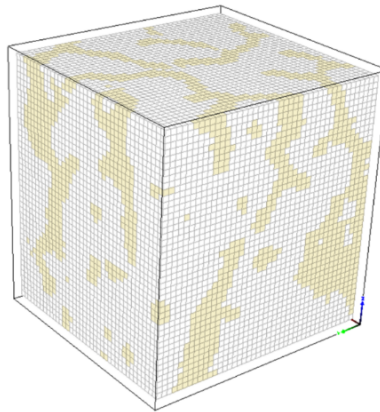

Figure 4. A 3D discretized of VTB-RUC.

were converted to approximately 72,000 equally shaped brick elements (subcells); see Figure 4. In situ material properties of each subcell representing bone wall were defined with the nonlinear R-O model with the material parameters found in Table 2, while subcells representing the marrow domain were set with very little stiffness. Then, the nonlinear with damage evolution response of the VTB-RUC was predicted using the incremental solution algorithm described above with a strain increment finite-size of $5 \cdot 10^{-4}$, presenting a sufficiently convergent criterion.

2.7. *Compression tests of printed polymeric VTB-RUC.* In order to generate the overall compression stress-strain response of a VTB-RUC manufactured from a polymeric material using a 3D-printer, compression tests were performed. The aim was to verify the ability of the calibrated nonlinear HFGMC to predict the tested response of a VTB-RUC behavior. Towards that goal, a 3D VTB-RUC solid model obtained from a μCT scan of a human cadaveric VTB (37 years old) was generated. Three printed polymeric VTB-RUC samples with a scale factor of 5:1 of the last 3D VTB-RUC with bottom and upper

parameters	notation	polymeric material	bone wall
elastic modulus	E (GPa)	2.56	11.00
Poisson ratio	v	0.35	0.3
material parameter	σ_0 (GPa)	0.060	0.110
material parameter	α	1	1
material parameter	n	5	5
strain-softening parameter	η	$1-\infty$	1.001
effective strength value	X (GPa)	0.060	0.110

Table 2. Material properties and model parameters for tested polymeric material and bone wall, calibrated and used in the analysis of the one-dimensional R-O relation: $\varepsilon = \sigma/E + \alpha(\sigma_0/E)(\sigma/\sigma_0)^n$.

caps were produced by a 3D printer. The volume fraction of the polymeric material in the VTB-RUC was 24.71%. In addition, three "dog-bone" specimens of the polymeric material were produced to measure the polymeric material response under tension. The experimental study was performed as follows: the "dog-bone" specimens were stretched using the Instron 5582 machine. Subsequently, compression tests were performed on the three polymeric 3D printed VTB-RUC samples. Initially, the VTB-RUC samples were cycled between two polished steel plates under reversed compression, three times nondestructively, between a 0 and 0.7% strain at a rate of 0.1 mm/min, followed by 10 minutes of relaxation. Subsequently, the samples were destructively compressed to a ∼3% strain at a rate of 0.1 mm/min (Figure 5a). The axial deformation (Figure 5b) was measured using the digital-image-correlation (DIC) method. The axial stress was defined as an instantaneous applied load divided by the cross-sectional area of the VTB-RUC. Strain was defined as an instantaneous deformation divided by the effective initial length between the steel plates. Subsequently, the measured results were compared with the nonlinear HFGMC model including a progressive damage analysis.
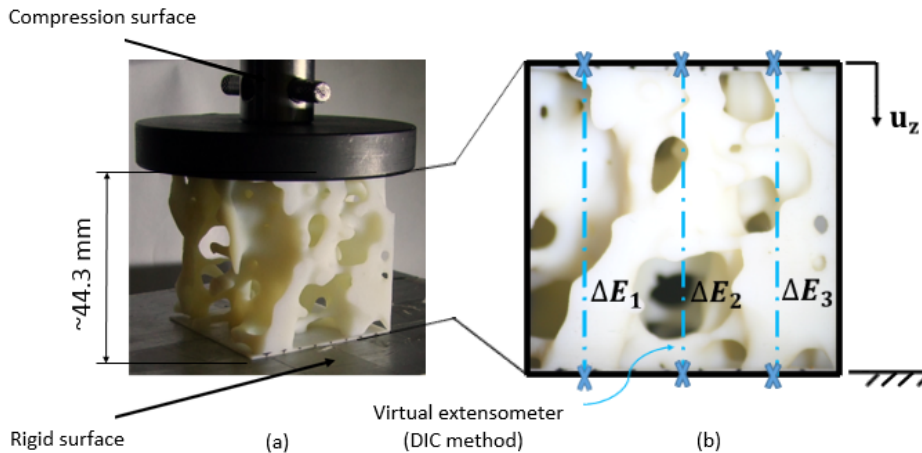
Figure 5. Experimental study: a compressed polymeric VTB-RUC highly porous microstructure, (a). An axial deformation gauge, (b).

3. Results and discussion

Figure 6 presents the experimental tension mechanical responses of the polymeric material used in this study. The material parameters of the R-O stress-strain relationship describing the nonlinear response of the polymeric material were calibrated (Table 2) and used in the analysis of the polymeric VTB-RUC samples to predict its nonlinear response with damage evolution.

The compression test results and the predicted HFGMC mechanical response with evolving damage of the polymeric VTB-RUC samples are shown in Figure 7. The effective strength value X of the polymeric material was calibrated at 0.06 GPa, while different values for the strain-softening parameter η were used to examine the ability to simulate energy dissipation rates. The above results provide an excellent agreement between the predicted and experimentally obtained nonlinear mechanical response of the polymeric VTB-RUC samples which began with an elastic region, followed by a nonlinear reversible response and continued with a nonlinear softening region caused by both the nonlinear elastic and damage. The experiments ceased after detecting the ultimate load. The predicted nonlinear response included postpeak strain-softening degradation behavior. This degradation was related to the strain-softening parameter η that controls the energy dissipation rate.

The predicted nonlinear with evolving damage responses of the available native VTB-RUCs compared with compression overloading tests available in the literature [Keaveny et al. 1999; Kopperdahl and Keaveny 1998] are shown in Figure 8. Bone volume fraction of the VTB-RUCs are also presented. The material parameters of the R-O constitutive relationship, effective strength value and parameter η were calibrated (Table 2) and used as the in situ nonlinear behavior of the bone wall phase in the VTB-RUCs.

The obtained mechanical responses were typical of the curves reported for the trabecular bone [Hayes and Carter 1976] and other natural and synthetic porous materials, such as cellular foams [Gibson and Ashby 1999]. Moreover, the predicted mechanical responses after the softening region presented another region of stiffening. When high compression closes the pores and cavities in the material, thus causing material stiffening, the consolidation region emerges [Gibson and Ashby 1999; Gibson et al. 2010].
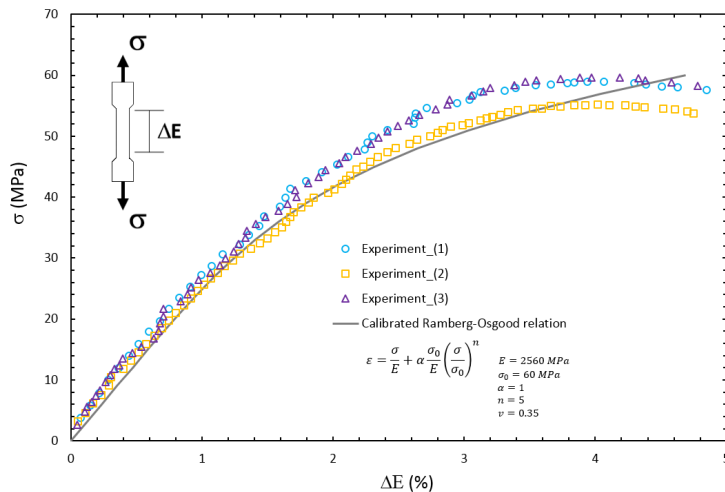
Figure 6. Mechanical response of the polymeric material used by the 3D printer.
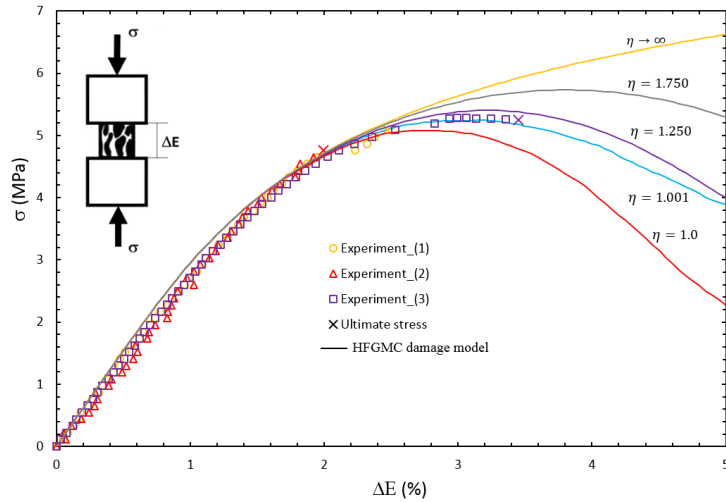
Figure 7. Experimental results of compressive loading and a predicted HFGMC mechanical responses with softening and evolving damage of a polymeric VTB-RUC highly porous microstructure.
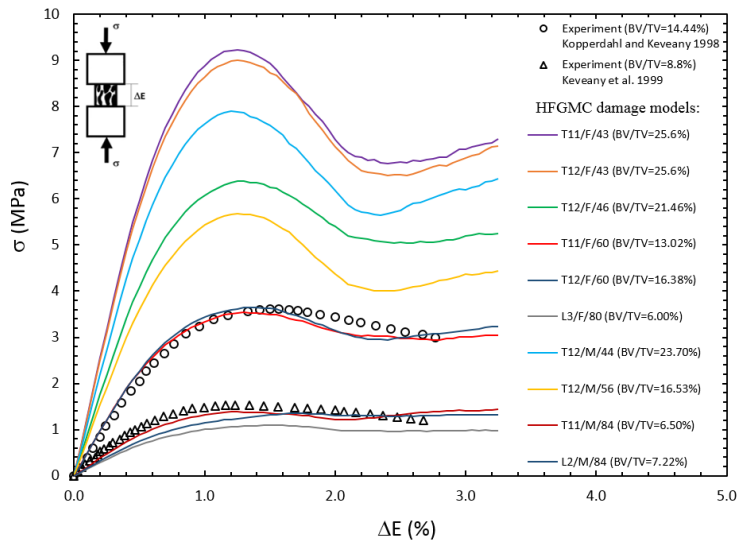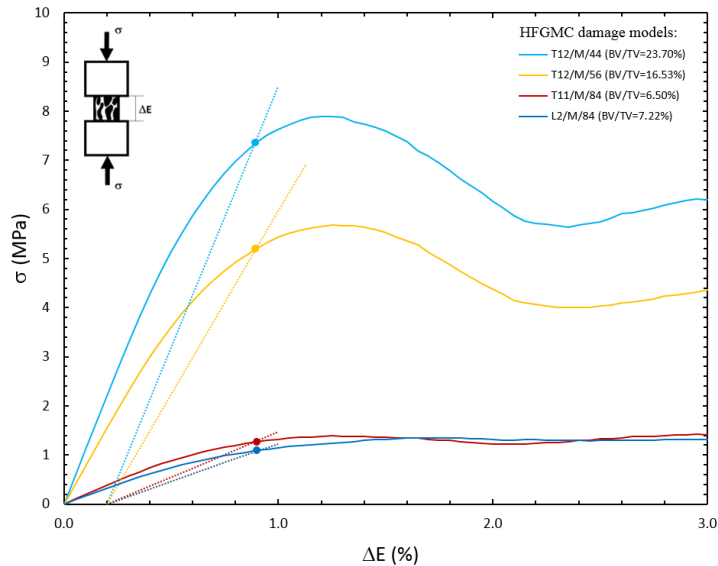

Figure 8. Predicted HFGMC mechanical responses vs. compression overloading tests of native VTBs available in the literature.

Figures 9 and 10 show the mechanical responses with yield points of the available native VTB-RUCs of the six VTB μCT scans of females and four scans of males with different vertebral levels (T11, T12, L3, and L4), respectively. The yield points were determined using a similar protocol proposed by Kopperdahl and Keaveny [1998]. In this study, the elastic modulus for each curve was computed based on all points up to 0.2% strain. The elastic slope was then used to construct 0.2% strain offset lines as shown in Figures 9 and 10. The intersections of the offset lines with the damage curves define the yield
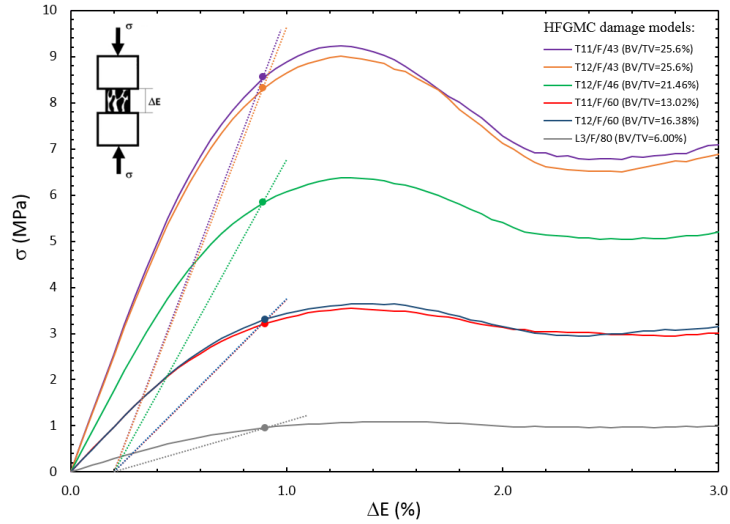
Figure 9. Predicted HFGMC mechanical responses for native female vertebral bones.

Figure 10. Predicted HFGMC mechanical responses for native male vertebral bones.

points. To this end, we present in Figures 11 and 12, respectively, the predicted yield stress and strain of the available native VTB-RUCs and compare these with the results found in the literature [Kopperdahl and Keaveny 1998]. Unlike the yield stresses for human VTBs, which demonstrated strong correlations with the bone volume fraction (BV/TV), the results of the yield strains were significantly independent of BV/TV. The above results strongly correspond with the previous outcomes indicating that for over-yielding behavior, the yield strains are independent of the apparent density and have reasonably constant values [Kopperdahl and Keaveny 1998]. Studies examining the independency of the compressive yield
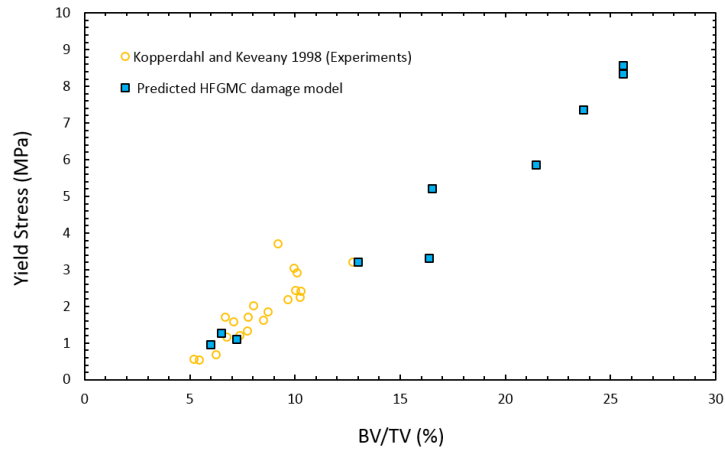
Figure 11. Predicted HFGMC yield stress vs. bone volume fraction of native VTBs.
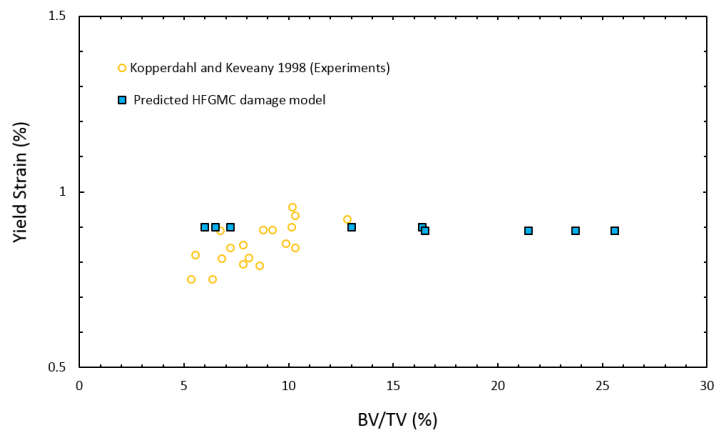
Figure 12. Predicted HFGMC yield strain vs. bone volume fraction of native VTBs.

strains to bone volume fractions have suggested that the failure of the highly porous trabecular bone microstructure is based on the strain [Gibson et al. 2010; Turner 1989].

4. Limitations

There are several limitations to the proposed approach seeking to generate a VTB nonlinear mechanical response. The first limitation is related to the acquisition accuracy of the μCT images. The relative Hounsfield Units (HUs) are associated with the full range of bone density all the way through the marrow medium. Thus, a threshold is used to determine whether a voxel is considered a bone wall or void. Therefore, we assumed that the μCT scans can represent the VTB microstructure and its porosity. The accuracy of these scans is a challenging problem, leading to errors in computing the microstructure and its bone volume fraction. Ultimately, this error in the RUC geometry can influence the computed mechanical response. Secondly, random bone variations and end fixtures may result in several errors and variation measurements resulting from in-vitro bone compression tests. These errors can be associated

with end-artifacts in the platen compression tests for trabecular bones [Keaveny et al. 1997]. Despite such limitations, we have adopted the same mechanical testing for the current polymeric VTB-RUC samples representing the microstructure of the VTB. Thirdly, periodic conditions of traction and displacement that may be imposed on the edges of the RUC can affect the predicted nonlinear behavior. In the current HFGMC model, the last periodic conditions were not applied. Fourthly, the porous media representing the marrow phase of the VTB was modeled with very little stiffness which might cause errors, especially for large cavities. Fifthly, small increments have to be used in the current nonlinear HFGMC incremental solution algorithm, which may be computationally expensive. A correction-algorithm suited for the micromechanical formulation can be developed to enhance computational efficiency. Sixthly, because of the limited availability of the experimental study for native human VTBs, it was difficult to calibrate the strain-softening parameter η that controls the energy dissipation rate of the native human VTB microstructure. More experimental and anisotropic damage modeling is needed to further develop the proposed progressive damage and better tailor it to different failure modes, such as local microbuckling and combined shear-compression modes, among others. The current damage parameter is isotropic with one damage parameter combining all these modes. Seventhly, this study concentrated on the compression analysis of the VTBs which mostly feature VTB failure; therefore, the characterization of tension-compression asymmetry [Kopperdahl and Keaveny 1998] is not investigated herein. Finally, the softening postpeak behavior will always be affected by mesh size unless a nonlocal interpolated solution variable and failure criteria are applied.

5. Conclusions

The parametric HFGMC micromechanics has been extended to include progressive damage of a highly porous microstructure such as VTB. The 3D nonlinear micromechanical modeling approach can predict the compression response of tested highly porous polymeric RUC. The proposed nonlinear HFGMC progressive damage micromodel was used to simulate compression failure of native VTB microstructures. Good predictive ability was shown for the compression yield stresses and strains compared to results reported in the literature. The proposed HFGMC VTB micromechanical damage analysis can be employed in future multiscale FE models of the macroscale vertebral bodies.

Acknowledgements

References

[Aboudi et al. 2013] J. Aboudi, S. M. Arnold, and B. A. Bednarcyk, *Micromechanics of composite materials: a generalized multiscale analysis approach*, 1st ed., Elsevier, Oxford, 2013.

[Chevalier et al. 2007] Y. Chevalier, D. Pahr, H. Allmer, M. Charlebois, and P. Zysset, "Validation of a voxel-based FE method for prediction of the uniaxial apparent modulus of human trabecular bone using macroscopic mechanical tests and nanoindentation", *J. Biomech.* **40**:15 (2007), 3333–3340.

[Cowin 2001] S. C. Cowin, *Bone mechanics handbook*, 2nd ed., Taylor & Francis, 2001.

[Fyhrie and Schaffler 1994] D. P. Fyhrie and M. B. Schaffler, "Failure mechanisms in human vertebral cancellous bone", *Bone* **15**:1 (1994), 105–109.

[Gibson and Ashby 1999] L. J. Gibson and M. F. Ashby, *Cellular solids: structure and properties*, 2nd ed., Cambridge University Press, 1999.

[Gibson et al. 2010] L. J. Gibson, M. F. Ashby, and B. A. Harley, *Cellular materials in nature and medicine*, Cambridge University Press, 2010.

[Goda and Ganghoffer 2015] I. Goda and J.-F. Ganghoffer, "3D plastic collapse and brittle fracture surface models of trabecular bone from asymptotic homogenization method", *Int. J. Eng. Sci.* **87** (2015), 58–82.

[Goda et al. 2012] I. Goda, M. Assidi, S. Belouettar, and J. F. Ganghoffer, "A micropolar anisotropic constitutive model of cancellous bone from discrete homogenization", *J. Mech. Behav. Biomed. Mater.* **16** (2012), 87–108.

[Goda et al. 2016] I. Goda, R. Rahouadj, J.-F. Ganghoffer, H. Kerdjoudj, and L. Siad, "3D couple-stress moduli of porous polymeric biomaterials using μCT image stack and FE characterization", *Int. J. Eng. Sci.* **100** (2016), 25–44.

[Haj-Ali and Aboudi 2009] R. Haj-Ali and J. Aboudi, "Nonlinear micromechanical formulation of the high fidelity generalized method of cells", *Int. J. Solids Struct.* **46** (2009), 2577–2592.

[Haj-Ali and Aboudi 2013] R. Haj-Ali and J. Aboudi, "A new and general formulation of the parametric HFGMC micromechanical method for two and three-dimensional multi-phase composites", *Int. J. Solids Struct.* **50** (2013), 907–919.

[Haj-Ali and Aboudi 2016] R. Haj-Ali and J. Aboudi, "Integrated microplane model with the HFGMC micromechanics for nonlinear analysis of composite materials with evolving damage", *Int. J. Solids Struct.* **90** (2016), 129–143.

[Haj-Ali and Kilic 2003] R. Haj-Ali and H. Kilic, "Nonlinear constitutive models for pultruded FRP composites", *Mech. Mater.* **35**:8 (2003), 791–801.

[Haj-Ali et al. 2014] R. Haj-Ali, H. Zemer, R. El-Hajjar, and J. Aboudi, "Piezoresistive fiber-reinforced composites: A coupled nonlinear micromechanical–microelectrical modeling approach", *Int. J. Solids Struct.* **51**:2 (2014), 491–503.

[Hambli 2013] R. Hambli, "Micro-CT finite element model and experimental validation of trabecular bone damage and fracture", *Bone* **56**:2 (2013), 363–374.

[Hamed and Jasiuk 2013] E. Hamed and I. Jasiuk, "Multiscale damage and strength of lamellar bone modeled by cohesive finite elements", *J. Mech. Behav. Biomed. Mater.* **28** (2013), 94–110.

[Harrison et al. 2013] N. M. Harrison, P. McDonnell, L. Mullins, N. Wilson, D. O'Mahoney, and P. E. McHugh, "Failure modelling of trabecular bone using a non-linear combined damage and fracture voxel finite element approach", *Biomech. Model. Mechanobiol.* **12** (2013), 225–241.

[Hayes and Carter 1976] W. C. Hayes and D. R. Carter, "Postyield behavior of subchondral trabecular bone", *J. Biomed. Mater. Res. A* **10**:4 (1976), 537–544.

[Keaveny et al. 1994] T. M. Keaveny, E. F. Wachtel, X. E. Guo, and W. C. Hayes, "Mechanical behavior of damaged trabecular bone", *J. Biomech.* **27**:11 (1994), 1309–18.

[Keaveny et al. 1997] T. M. Keaveny, E. F. Morgan, and O. C. Oscar, *Bone mechanics*, edited by M. Kuts, McGraw-Hill, 1997.

[Keaveny et al. 1999] T. M. Keaveny, E. F. Wachtel, and D. L. Kopperdahl, "Mechanical behavior of human trabecular bone after overloading", *J. Orthop. Res.* **17**:3 (1999), 346–353.

[Keaveny et al. 2003] T. M. Keaveny, T. P. Pinilla, R. P. Crawford, D. L. Kopperdahl, and A. Lou, "Systematic and random errors in compression testing of trabecular bone", *J. Orthop. Res.* **15**:1 (2003), 101–110.

[Khan and Huang 1995] A. S. Khan and S. Huang, *Continuum Theory of Plasticity*, Wiley, New York, 1995.

[Kopperdahl and Keaveny 1998] D. L. Kopperdahl and T. M. Keaveny, "Yield strain behavior of trabecular bone", *J. Biomech.* **31** (1998), 601–608.

[Maquer et al. 2015] G. Maquer, S. N. Musy, J. Wandel, T. Gross, and P. K. Zysset, "Bone volume fraction and fabric anisotropy are better determinants of trabecular bone stiffness than other morphological variables", *J. Bone Miner. Res.* **30**:6 (2015), 1000–1008.

[Nevitt et al. 1999] M. C. Nevitt, P. D. Ross, L. Palermo, T. Musliner, H. K. Genant, and D. E. Thompson, "Association of prevalent vertebral fractures, bone density, and alendronate treatment with incident vertebral fractures: effect of number and spinal location of fractures", *Bone* **25**:5 (1999), 613–619.

[Niebur et al. 2000] G. L. Niebur, M. J. Feldstein, J. C. Yuen, T. J. Chen, and T. M. Keaveny, "High-resolution finite element models with tissue strength asymmetry accurately predict failure of trabecular bone", *J. Biomech.* **33**:12 (2000), 1575–1583.

[Rockoff et al. 1969] S. D. Rockoff, E. Sweet, and J. Bleustein, "The relative contribution of trabecular and cortical bone to the strength of human lumbar vertebrae", *Calcif. Tissue Res.* **3**:1 (1969), 163–175.

[Turner 1989] C. H. Turner, "Yield behavior of bovine cancellous bone", *J. Biomech. Eng.* (*ASME*) **111**:3 (1989), 256–260.

[Wolfram et al. 2011] U. Wolfram, H.-J. Wilke, and P. K. Zysset, "Damage accumulation in vertebral trabecular bone depends on loading mode and direction", *J. Biomech.* **44**:6 (2011), 1164–1169.

[Zysset 1994] P. Zysset, *A constitutive law for trabecular bone*, École Polytechnique Fédérale de Lausanne, Lausanne, Switzerland, 1994.

EYASS MASSARWA: eyassmas@post.tau.ac.il
Faculty of Engineering, Tel-Aviv University, 69978 Tel-Aviv, Israel

JACOB ABOUDI: aboudi@eng.tau.ac.il
Faculty of Engineering, Tel-Aviv University, 69978 Tel-Aviv, Israel

FABIO GALBUSERA: fabio.galbusera@uni-ulm.de
Department of Spine Surgery III, IRCCS Galeazzi Orthopaedic Institute, Via Riccardo Galeazzi 4, 20161 Milan, Italy

HANS-JOACHIM WILKE: hans-joachim.wilke@uni-ulm.de
Institute for Orthopedic Research and Biomechanics, Ulm University, Helmholtzstrasse 14, D-89081 Ulm, Germany

RAMI HAJ-ALI: rami98@tau.ac.il
Faculty of Engineering, Tel-Aviv University, 69978 Tel-Aviv, Israel

JOURNAL OF MECHANICS OF MATERIALS AND STRUCTURES

msp.org/jomms

Founded by Charles R. Steele and Marie-Louise Steele

Cover photo: Mando Gomez, www.mandolux.com